

This work was written as part of one of the author's official duties as an Employee of the United States Government and is therefore a work of the United States Government. In accordance with 17 U.S.C. 105, no copyright protection is available for such works under U.S. Law.

Public Domain Mark 1.0

<https://creativecommons.org/publicdomain/mark/1.0/>

Access to this work was provided by the University of Maryland, Baltimore County (UMBC) ScholarWorks@UMBC digital repository on the Maryland Shared Open Access (MD-SOAR) platform.

Please provide feedback

Please support the ScholarWorks@UMBC repository by emailing scholarworks-group@umbc.edu and telling us what having access to this work means to you and why it's important to you. Thank you.

RESEARCH ARTICLE

10.1002/2013JD021423

Key Points:

- Determine contributions of aerosols/cirrus to measured hyperspectral data
- Differences in derivative spectra permit detecting low optical thickness cirrus
- Spectral derivatives are valuable for atmospheric remote sensing

Correspondence to:

R. A. Hansell,
Richard.A.Hansell@nasa.gov

Citation:

Hansell, R. A., S.-C. Tsay, P. Pantina, J. R. Lewis, Q. Ji, and J. R. Herman (2014), Spectral derivative analysis of solar spectroradiometric measurements: Theoretical basis, *J. Geophys. Res. Atmos.*, 119, 8908–8924, doi:10.1002/2013JD021423.

Received 23 DEC 2013

Accepted 17 JUN 2014

Accepted article online 21 JUN 2014

Published online 21 JUL 2014

Spectral derivative analysis of solar spectroradiometric measurements: Theoretical basis

R. A. Hansell^{1,2}, S.-C. Tsay², P. Pantina^{2,3}, J. R. Lewis^{2,4}, Q. Ji^{2,5}, and J. R. Herman^{2,4}
¹Earth System Science Interdisciplinary Center, University of Maryland, College Park, Maryland, USA, ²NASA Goddard Space Flight Center, Greenbelt, Maryland, USA, ³Science Systems and Applications Inc., Lanham, Maryland, USA, ⁴Joint Center for Earth Systems Technology, University of Maryland, Baltimore County, Maryland, USA, ⁵Sigma Space Corp., Greenbelt, Maryland, USA

Abstract Spectral derivative analysis, a commonly used tool in analytical spectroscopy, is described for studying cirrus clouds and aerosols using hyperspectral, remote sensing data. The methodology employs spectral measurements from the 2006 Biomass-burning Aerosols in Southeast Asia field study to demonstrate the approach. Spectral peaks associated with the first two derivatives of measured/modeled transmitted spectral fluxes are examined in terms of their shapes, magnitudes, and positions from 350 to 750 nm, where variability is largest. Differences in spectral features between media are mainly associated with particle size and imaginary term of the complex refractive index. Differences in derivative spectra permit cirrus to be conservatively detected at optical depths near the optical thin limit of ~ 0.03 and yield valuable insight into the composition and hygroscopic nature of aerosols. Biomass-burning smoke aerosols/cirrus generally exhibit positive/negative slopes, respectively, across the 500–700 nm spectral band. The effect of cirrus in combined media is to increase/decrease the slope as cloud optical thickness decreases/increases. For thick cirrus, the slope tends to 0. An algorithm is also presented which employs a two model fit of derivative spectra for determining relative contributions of aerosols/clouds to measured data, thus enabling the optical thickness of the media to be partitioned. For the cases examined, aerosols/clouds explain $\sim 83\%/17\%$ of the spectral signatures, respectively, yielding a mean cirrus cloud optical thickness of 0.08 ± 0.03 , which compared reasonably well with those retrieved from a collocated Micropulse Lidar Network Instrument (0.09 ± 0.04). This method permits extracting the maximum informational content from hyperspectral data for atmospheric remote sensing applications.

1. Introduction

Over the years, derivative analysis has been used extensively in analytical spectroscopy for discerning subtle changes in the spectral shapes of organic materials [O'Haver and Green, 1976]. Consequently, this has proven to be a valuable tool in pharmacology and biomedicine [e.g., Bellisola and Sorio, 2012]. This technique has also been more recently applied to nadir-viewing, hyperspectral remote sensing measurements in the geosciences, yielding valuable information on the scattering and absorption properties of the target media. Examples of applications that have employed this approach include ocean color monitoring and crop stress detection using Hyperspectral Imager for the Coastal Ocean [Tufillaro and Davis, 2012] and Airborne Visible/Infrared Imaging Spectrometer [Estep and Carter, 2005] measurements, respectively. A review of published literature reveals that there are very limited applications of this technique that focus exclusively on Earth's atmosphere, particularly with respect to using high spectral resolution data. Earlier work exploited spectral curvature information found in multispectral, ground-based measurements for partitioning fine/coarse mode aerosols [e.g., O'Neill et al., 2003], while others employed derivative analysis for removing atmospheric effects to detect surface targets [e.g., Philpot, 1991]. The aim of this study is to apply the principles of derivative spectroscopy to hyperspectral ground-based data for investigating the spectral signatures of aerosols and cirrus clouds. Higher spectral resolution provides a greater opportunity for probing the fine optical structure of the medium, which may not be possible using discrete, narrowband channels.

Tsai and Philpot [1998] discuss in detail the methods and caveats of derivative analysis for studying high-resolution, spectrally continuous, remote sensing data. The current work builds on these methods for applications in the atmospheric sciences. To demonstrate the utility of this approach, we take advantage of comprehensive ground-based measurements from the NASA's Surface-based Mobile Atmospheric Research & Testbed

Laboratories (cf. <http://smartlabs.gsfc.nasa.gov/>) during the 2006 (26 February–5 May) BASE-ASIA (Biomass-burning Aerosols in Southeast Asia: Smoke Impact Assessment) field campaign [Lin *et al.*, 2013; Tsay *et al.*, 2013] in Phimai Thailand (15.183°N, 102.565°E). Biomass-burning smoke aerosols pervade much of Southeast Asia (SEA) [Hyer *et al.*, 2013; Tsay *et al.*, 2013] and are often found to coexist with cirrus clouds [Tsay *et al.*, 2013]. Consequently, this region has been a major focus of research including the study of thin cirrus contamination in aerosol retrievals [e.g., Chew *et al.*, 2011; Huang *et al.*, 2011, 2012, 2013], the assessment of aerosol direct radiative effects [e.g., Hsu *et al.*, 2003], and the study of aerosol-cloud interactions [Lin *et al.*, 2014]. Hereafter, all the spectral measurements, unless otherwise noted, are considered to be hyperspectral and measured at the surface.

Previous work has shown the successful application of using longwave IR spectral measurements for studying cirrus clouds and aerosols [e.g., Guo *et al.*, 2005; Yang *et al.*, 2005; Hansell *et al.*, 2008, 2010, 2012]. However, since the signal-to-noise ratio (SNR) is stronger at shorter wavelengths due to scattered solar radiances, this study focuses exclusively on the visible shortwave IR (SWIR) spectral region. Shortwave spectral measurements have already been used for studying liquid water clouds [e.g., McBride *et al.*, 2011] and for quantifying cloud and surface effects [Rabette and Pilewskie, 2002]. A review of the literature seems to suggest that applying spectroscopic methods to ground-based, high spectral resolution SWIR data for studying cirrus clouds and aerosols have not yet been conducted. It is therefore within this framework that the current study was designed. Motivated by earlier works, and the availability of an extensive data set, the main objectives are to

1. investigate the sensitivity of ground-based solar spectroradiometric measurements to cirrus and aerosols,
2. apply derivative analysis to partition cirrus cloud optical thickness (COT) from retrieved aerosol optical thickness (AOT) measurements, and
3. validate results using retrieved COTs from a collocated Micropulse Lidar (MPL).

In short, we explore ways by which spectroscopic techniques can be employed for hyperspectral remote sensing of atmospheric particles.

To address these objectives, the theoretical basis is first discussed, followed by model sensitivity studies to examine the spectral characteristics of cirrus and aerosols. A demonstration of the derivative technique is then presented using selected aerosol-cirrus cases from BASE-ASIA identified from the Micropulse Lidar Network (MPLNET) [Welton *et al.*, 2001], Aerosol Robotic Network (AERONET) [Holben *et al.*, 1998], and Moderate Resolution Imaging Spectroradiometer (MODIS) MOD06 [Platnick *et al.*, 2003] data. This study adopts the commonly used classifications for cirrus in terms of COT [Sassen and Cho, 1992]: subvisual ($\tau_c < 0.03$), thin ($0.03 < \tau_c < 0.3$), and opaque ($\tau_c > 0.3$). We extend our analysis of the sensitivity of measured spectra to COT within a span of 0.01–1.0 to evaluate the extent to which the spectral content of the signal can be exploited for partitioning cirrus from aerosols.

During BASE-ASIA, forest fires to the north of Phimai near Myanmar, Laos, and Northern Thailand (e.g., Chiang Mai—18.795°N, 98.998°E) resulted in relatively high particulate matter (PM) 10 surface concentrations (e.g., $PM_{10} \sim 100 \mu g m^{-3}$), with peak intensities noted in March 2006 [Li *et al.*, 2013]. However, due to prevailing winds from the south, Phimai experienced lower PM_{10} levels ($\sim 33 \pm 13 \mu g m^{-3}$), indicating smaller contributions of smoke aerosols from the burning events. Observed aerosols in Phimai were primarily from regional agricultural fires (e.g., open burning of rice straw) and industrial/traffic emissions from nearby metropolitan areas [Li *et al.*, 2013]. The spectral features associated with biomass-burning smoke and urban pollutants are examined to partition their roles from that of cirrus in the spectral measurements.

Critical to this work are high-frequency measurements from a solar spectroradiometer (Analytical Spectral Devices (ASD) FieldSpec Pro, PANalytical Inc., <http://www.asdi.com>), which yielded ~ 2 months of highly resolved spectral fluxes ($\lambda = 350$ –2500 nm). The ASD has been previously used in absolute radiometric calibration studies [Kindel *et al.*, 2001] and for acquiring spectral surface reflectance measurements for characterizing the optical properties of soils, vegetation, etc. [e.g., Bassani *et al.*, 2009; Clevers *et al.*, 2010]. Details of the ASD and its measurements for this study are provided in section 2.

The paper is arranged as follows: Section 2 presents the observations and models used, followed by a description of the methodology in section 3. Next, sensitivity studies of the spectral characteristics of aerosols and cirrus are given in section 4. A demonstration of the derivative technique is then presented in section 5

Table 1. Primary Measurements

Instrument	Model	Measurement	Usage
Pyroheliometer ^a	NIP	solar flux	constrain solar spectral data
Spectrometer	ASD	solar spectral flux	simulated by model
Sun photometer	Cimel	AOT at 0.34, 0.38, 0.44, 0.5, 0.67, 0.87, and 1.02 μm ; PWV ^b	model's AOT and total column water vapor inputs
Lidar	MPL	NRB profiles	model's input—infer aerosol profile/cloud height
Imager	Total Sky Imager	sky image	cloud identification
MODIS	-	MOD06 cloud properties	COT used as model constraint

^aCross comparison.

^bPWV = precipitable water vapor.

using selected aerosol-cirrus cases. Lastly, results and uncertainties are examined in section 6, with concluding remarks given in section 7.

2. Observations and Models

2.1. Instruments and Measurements

Among the primary measurements considered in this study (Table 1), spectral and broadband direct-normal solar fluxes were observed, respectively, using an ASD mounted on a Kipp and Zonen solar tracker (model 2AP) directly alongside an Eppeley Normal Incident Pyroheliometer (NIP: <http://www.eppley.com>). The spectral range of the ASD is from $\lambda = 350$ –2500 nm with a nominal 1 nm spectral resolution. The NIP, on the other hand, is a broadband radiometric instrument that covers the wavelength range $\lambda = 280$ –2800 nm. The ASD uses

three detectors: a 512 element silicon photodiode array for the spectral region $\lambda = 350$ –1000 nm (visible near IR), and graded index, thermal electrically cooled, extended range InGaAs photodiodes for the spectral regions $\lambda = 1000$ –1830 nm (SWIR1) and $\lambda = 1830$ –2500 nm (SWIR2).

As shown in Figure 1a, the configuration of the ASD fore optic consists of a manufacture-provided Direct Irradiance Attachment (DIA), with a field of view (FOV) of 1.5° that is connected to a full-sky flux remote cosine receptor (RCR). A cutaway of the RCR directly interfaces to the spectrometer via a fiber optic assembly (Figure 1b). This arrangement allows for continuous direct-normal solar flux measurements to be made while tracking the Sun. Hence, in this configuration, the instrument behaves as a spectroradiometer, similar in principle to the Solar Spectral Flux Radiometer [Pilewskie *et al.*, 2003]. With the RCR attached, the manufacturer performs a radiometric calibration to convert raw measurements into spectral fluxes.

For consistency, this study compares the ASD's integrated flux against that measured by a collocated NIP

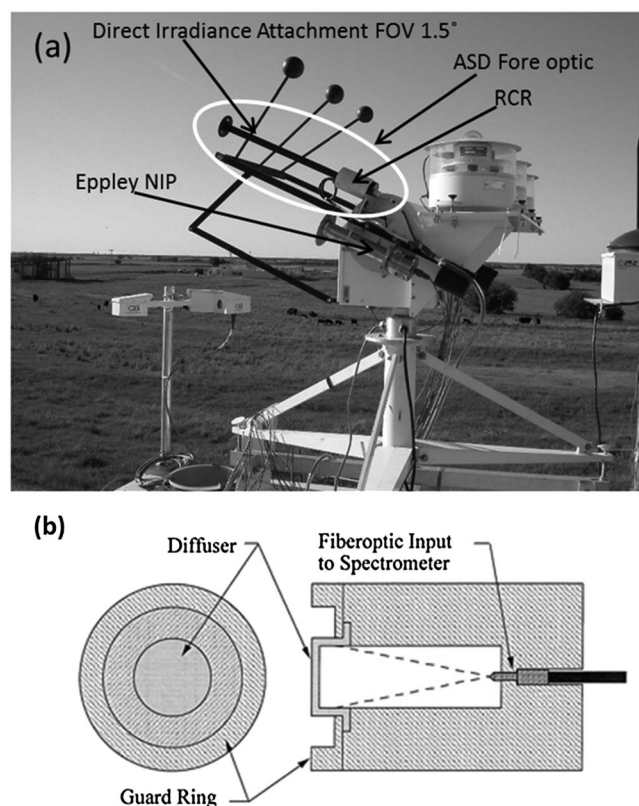


Figure 1. (a) Shown, for illustrative purposes only, are the ASD (circled region) and Eppeley NIP mounted to the Kipp and Zonen 2AP solar tracker. A Direct Irradiance Attachment (DIA) which restricts the angular FOV to 1.5° mounts to the full-sky flux remote cosine receptor (RCR). (b) Illustration depicting the ASD RCR that interfaces to the spectrometer's fiber optic assembly (figure courtesy of PANalytical).

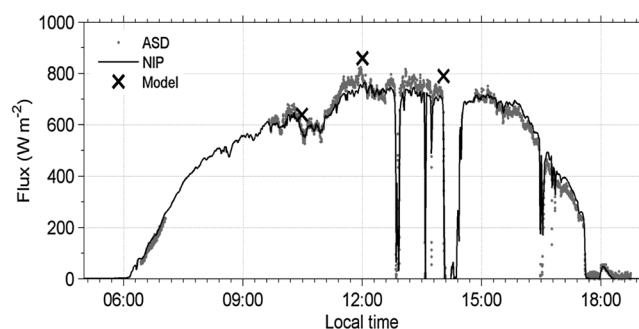


Figure 2. The diurnal variability in the total measured flux (W m^{-2}) as measured by the ASD (gray markers) and NIP (solid black line) for cirrus case 3 May 2006. Note that the two data sets are well correlated with each other, with absolute differences attributed to the inherent thermal characteristics of the NIP [Ji *et al.*, 2011]. Also shown for reference are calculated fluxes for the same day.

effect present in broadband radiometers [Ji *et al.*, 2011]. Using the MODTRAN radiative transfer code (section 2b), spectral fluxes were calculated for 3 May 2006 and then integrated across the ASD spectral domain. Figure 2 shows the resulting fluxes (black "x") for comparison, which interestingly enough, shows better agreement with the ASD than with the NIP. This is because the ASD is not affected by thermal noise [Ji *et al.*, 2011].

2.2. Radiative Transfer and Optical Models

For this study, MODTRAN (v.5.2.0.0) was used to simulate the ASD spectral fluxes for wavelengths spanning $\lambda = 300\text{--}2500$ nm. MODTRAN [Anderson *et al.*, 2009; Berk *et al.*, 2006, 2008] is a narrowband atmospheric radiative transfer model (RTM) that has been used extensively [e.g., French *et al.*, 2003]. The model's spectroscopic data are based on the high-resolution transmission molecular absorption 2008 line compilation [Rothman *et al.*, 2009]. The model atmosphere is horizontally homogeneous and allows user-defined clouds and aerosols to be located at prescribed heights. A climatological tropical atmospheric profile [Anderson *et al.*, 1986] is employed for all simulations, with solar and viewing geometry settings (i.e., solar and sensor zenith angles) constrained using the time stamps of the ASD spectral measurements. Geolocation and altitude data for Phimai were also used as model input. The model's total precipitable water was scaled 1.2 times to match regional column water vapor amounts (~ 4.2 cm) during the deployment period. Sensitivity of derived COTs to column water vapor is addressed later in section 6. Spectral fluxes (in units of $\text{W m}^{-2} \text{ nm}^{-1}$) were generated using MODTRAN's 5 cm^{-1} resolution molecular band model, convolved to the Gaussian slit function of the ASD and then linearly interpolated to the spectral domain of the instrument for subsequent analysis.

Cloud optical properties used to characterize ice particles in this study were derived from MODTRAN's subvisual/standard cirrus models ($4 \mu\text{m}/64 \mu\text{m}$ mode radii, respectively), with user-prescribed inputs of cloud geometrical thickness (km), cloud base altitude (km; relative to sea level), and $0.55 \mu\text{m}$ layer extinction (km^{-1}). Default cloud thickness, base altitude, and profile extinction for the subvisual/standard models are 0.2 km , 11.0 km , 0.028 km^{-1} / 1.0 km , 11.0 km , and 0.14 km^{-1} , respectively. Both are based on Mie solutions assuming a lognormal size distribution. A $10 \mu\text{m}$ effective diameter (D_{eff}) ice cloud bulk scattering model, commonly employed in Terra/Aqua MODIS studies [Baum *et al.*, 2011] was also used (http://www.ssec.wisc.edu/~baum/Cirrus/Solar_Spectral_Models.html). The model spans the wavelengths $\lambda = 0.40\text{--}2.2 \mu\text{m}$ with a resolution of $0.01 \mu\text{m}$. A D_{eff} of $10 \mu\text{m}$ was chosen, since most sampled ice crystals that characterize optically thin cirrus, common for the SEA region, have size distributions that are generally within $10 \mu\text{m}$ [Heymsfield and Jahnsen, 1974].

Based on MPL (532 nm) normalized relative backscatter (NRB) profiles (section 5) and data from the MPLNET cloud detection and classification algorithm [e.g., Campbell *et al.*, 2008; J. R. Lewis *et al.*, Overview and analysis of the MPLNET version 3 cloud detection algorithm, manuscript in preparation, 2014], high-level cirrus were commonly found at altitudes (H) of $\sim 11\text{--}15 \text{ km}$ with cloud thicknesses (ΔZ) between 0.5 and 1.0 km . This is consistent with those identified from other field experiments near the tropics [e.g., McFarquhar *et al.*, 2000]. For this study, a range of COTs ($0.01\text{--}1.0$) that spans the optical regimes for cirrus (subvisual, thin, and opaque) [Sassen and Cho, 1992] was used.

The aerosol models in this study were selected based on their representativeness of biomass-burning smoke and regional pollutants. Li *et al.* [2013] found organic matter and sulfate to be the most dominant aerosols in

calibrated by Eppley Laboratory. For reference, the NIP has a FOV of $\sim 5.7^\circ$. A scale factor is applied to each ASD channel (2151 total channels), accounting for the restricted FOV by the instrument's DIA. Figure 2 shows the comparison between the integrated/scaled ASD spectra and coincident NIP flux measurements for one of the cirrus cases used in this study (3 May 2006; section 5). Both instruments were collocated on a solar tracker, and their FOVs are both larger than the angular size of the solar disk ($\sim 0.5^\circ$). Therefore, discrepancies in the measurements are likely attributable to the inherent thermal

Table 2. MODTRAN Inputs

Parameter	Source	Comment
Location	Observations	Phimai Observatory ^a
Atmospheric profile	Model	Tropical profile
Solar incident angle	Observations	Derived from location/time of ASD measurements
Aerosol optical thickness	Observations	AERONET Sun photometer ($\lambda = 0.55 \mu\text{m}$)
Water vapor	Model/Observations	Scaled atmospheric profile to match measurements
Aerosols	Literature/Observations	Several sources employed in the study ^b
Aerosol distribution	MPL/model ^c	
Clouds	Model/Literature/Observations ^d	
Surface albedo	Literature	Spectral measurements not sensitive to albedo

^aLongitude 102.565°E, latitude 15.183°N; 230 m above sea level.

^bOPAC aerosols, BB model [Carr, 2005], and AERONET derived properties at Phimai.

^cMPL provides reference for aerosol distribution in model.

^dMODTRAN cirrus models, bulk cirrus model from ice scattering database, and MOD06-retrieved cloud COT.

Phimai during BASE-ASIA. Mostly occurring in the fine mode, the total mass of these particles ($\text{PM}_{2.5}$) accounted for nearly 70% of the measured PM_{10} —similar to what was found in nearby metropolitan areas—and likely attributable to vehicular emissions. The variable nature of soot in this region ($\sim 3.0\text{--}9.4 \mu\text{g m}^{-3}$), reported in other studies [e.g., Kim Oanh *et al.*, 2006; Sahu *et al.*, 2011], suggests that it can contribute to local aerosol loading. To account for urban aerosols, we used a soot model based on the refractive indices of Shettle and Fenn [1979]. Note that the latter data were based on a study of the refractive index of carbonaceous materials [Twitty and Weinman, 1971]. Additional aerosol models from the Optical Properties of Aerosols and Clouds (OPAC) database [Hess *et al.*, 1998] were also employed, including sulfate, elemental carbon, as well as insoluble and water-soluble components. Since average relative humidity (RH) was $\sim 65\%$ during the experiment, the hygroscopic properties of aerosols were important. Consequently, these aerosols were examined using OPAC-provided data under variable RH conditions (50%, 70%, and 90%).

We also employed a user-defined smoke model from Carr, 2005, hereinafter referred to as the biomass-burning (BB) model, for simulating biomass-burning aerosols. It consists of a mixture of organic matter, elemental carbon (soot), and water-soluble compounds and was originally developed to represent smoke aerosols in Jabiru, Australia. Similar aerosols were also reported in the SEA region during previous studies [Li *et al.*, 2013]; hence, the BB model serves as a reasonable proxy for demonstration purposes in the current work. Regional differences in particle properties will result in model uncertainties.

Lastly, an aerosol model based on AERONET-retrieved optical properties at Phimai was used. Although aerosols are rarely spherical, Mie-calculated single-scattering properties (i.e., single-scattering albedo, asymmetry parameter, and extinction coefficient) were used for all the OPAC and soot aerosols for simplicity. The spectral properties were calculated from $\lambda = 0.2\text{--}2.5 \mu\text{m}$ and then integrated over particle sizes centered about a fine-mode peak of $\sim 0.1 \mu\text{m}$. Measured number/volumetric size distributions during BASE-ASIA peaked around $0.1 \mu\text{m}/0.33 \mu\text{m}$, respectively [Li *et al.*, 2013]. The BB and AERONET models' single-scattering properties are from Carr [2005] and AERONET retrievals, respectively. All AOTs are defined at $0.50 \mu\text{m}$. Consistent with MPL observations, all aerosols were defined as boundary layer aerosols in the RTM, where inputs (Table 2) were constrained by measurements during the field experiment and available data from the literature.

3. Methodology: Derivative Spectral Analysis

Detailed changes in observed flux can be difficult to discern in a zeroth-order spectrum. However, spectral derivatives can facilitate identifying subtle changes in flux resulting from aerosol and cloud extinction. Hence, derivative spectra can be linked to scattering and absorption processes in the atmosphere that are mainly functions of particle size and complex refractive index. Although higher-order derivatives (order >2) have been useful in spectroscopy [e.g., Butler and Hopkins, 1970], the current study employs the first two derivatives, as these likely contain the signal's maximum spectral content.

Since derivative spectra are sensitive to noise, a smoothing algorithm is needed to optimize the SNR. Here the commonly used Savitzky–Golay algorithm [Savitzky and Golay, 1964] is employed, where a 31 nm wide moving filter is applied to both modeled and measured data using a second-order polynomial fit within the

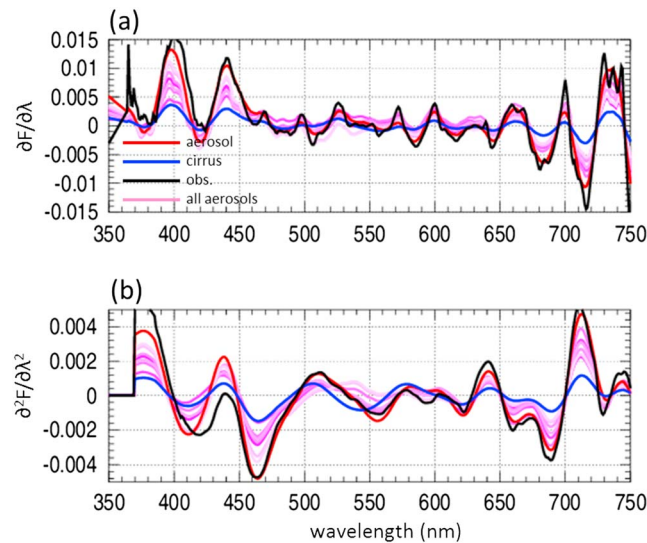


Figure 3. Smoothed (a) first- and (b) second-order derivative spectra for both observed (observations: black) and modeled (cirrus/aerosols) data ($\lambda = 350\text{--}750$ nm), where variability in the measurements is largest. Cirrus and aerosols are marked by the blue and red/magenta curves, respectively. Positive peaks, which denote maximal change in spectral flux, correspond to the wavelengths employed in the fitting algorithm. Magnitude and phase differences between spectra are evident, owing to the diverse physicochemical properties in the media.

derivatives of flux, F . First- and second-order derivatives can be computed, respectively, as

$$\left[\frac{\partial F}{\partial \lambda} \right]_i \approx \frac{F(\lambda_i) - F(\lambda_j)}{\Delta \lambda} \quad (1)$$

$$\left[\frac{\partial^2 F}{\partial \lambda^2} \right]_j = \frac{\partial}{\partial \lambda} \left[\frac{\partial F}{\partial \lambda} \right]_j \approx \frac{F(\lambda_i) - 2F(\lambda_j) + F(\lambda_k)}{(\Delta \lambda)^2} \quad (2)$$

where $\lambda_i < \lambda_j < \lambda_k$ and bandwidth $\Delta \lambda$ (i.e., sampling interval) control the degree of detail extracted from the spectra. For first derivatives, a narrow bandwidth ($\Delta \lambda \leq 5$ nm) reasonably captured changes in the transmitted flux of cirrus clouds and aerosol. Because the risk of losing spectral details increases as larger sampling intervals are used, a $\Delta \lambda$ of 1 nm was chosen for this study to demonstrate the methodology. With higher-order derivatives, the SNR decreases. Therefore, bandwidth $\Delta \lambda$ must be increased to improve the signal content. Consequently, for second derivatives, a $\Delta \lambda$ of 20 nm was selected. Optimization schemes for selecting desired sampling widths in atmospheric data sets will be further explored in future work. Examples of derivative spectra are discussed below.

Lastly, positive peaks of the derivative spectra were identified by searching for their associated downward zero crossings. These locations mark the wavelengths at which one can expect maximum change in spectral flux to occur for aerosols and cirrus. Consequently, the algorithm uses these points in the spectral fitting across the range $\lambda = 350\text{--}750$ nm, where variability is largest (details are discussed in section 4). Examples of smoothed first- and second-order derivative spectra for ASD measurements and modeled data (cirrus and aerosol), with the noted positive peaks, are presented in Figure 3. It is worth pointing out the magnitude and phase differences between the spectra, particularly from ~ 500 to 700 nm. The first derivative spectrum for cirrus, for example, is relatively flat, whereas for aerosol, there are many marked features likely attributable to the diverse chemical makeup of aerosols versus ice. A shift in peak positions (~ 10 nm) between cirrus and aerosol/ASD observations is also evident in the second derivative spectrum around 500 nm. These subtle differences between spectra yield important clues for fingerprinting atmospheric media.

The flux spectrum, $F_{\text{tot}}(\lambda)$, can be decomposed into its component parts by assuming that it is a weighted, linear combination of aerosols and clouds over the spectral range of the instrument. By exploiting the

filter window. For higher-order spectra, noise becomes amplified. Hence, to improve the fit, the width of the filter window is increased to 71 nm or about 2 times larger. The smoothing parameters were adjusted to maximize the spectral content of the data without suppressing key features. Note that the modeled data are smoothed since the media's extinction coefficients only cover discrete spectral points (i.e., they are not continuous). We also point out that there is a balance between noise reduction and the spectral resolution of the data. For example, a large reduction in noise could conceivably remove important subscale absorption features. However, a lower SNR will likely bias the derivative spectra, thus rendering the technique ineffectively. The effects of applying different smoothing algorithms are detailed by Tsai and Philpot [1998].

After smoothing, a finite divided difference approximation is used to compute the n th-order spectral

shorter wavelengths ($\lambda = 350\text{--}750\text{ nm}$), the effects of strong water vapor absorption and low SNR in the measurements at the longer wavelengths (Figure 7) are removed. Weighting factors, (w), denote the relative significance of each component taking on the values of either 0 or 1 depending on the modeled-measured differences in the first and second derivatives. The form of the observed spectrum is given by

$$F_{\text{tot}}(\lambda) = \sum_{i=1}^n (w(a)_i \cdot F(a)_i + w(c)_i \cdot F(c)_i), \quad (3)$$

where the summation is solved over the total number (n) of wavelengths corresponding to the positive peak positions in the derivative spectra. The aerosol (a) and cirrus (c) contributions are given by the first and second terms, respectively. Note that wavelength dependence is implicit in both terms (w_{λ} and F_{λ}). The partitioning methodology employed is analogous to determining how much variability in the measured spectrum can be explained by the individual component parts such that

$$\% \text{aerosol} = \frac{\sum_{i=1}^n w(a)_i}{n} \quad (4)$$

$$\% \text{cirrus} = \frac{\sum_{i=1}^n w(c)_i}{n} \quad (5)$$

Statistical significance testing of computed derivatives between the cirrus and aerosol modeled data shows all model combinations to be statistically significant at the 99% confidence level ($\alpha = 0.01$) using a two-tailed Student's t test. Here the t statistic is defined as

$$t = \frac{m_a - m_c}{\sqrt{(E_a)^2 + (E_c)^2}}, \quad (6)$$

where m_a/m_c are the averaged derivatives for the aerosol/cirrus models, respectively. The denominator is the standard error of the slope differences, with E_a/E_c being the respective standard errors of each component. In the presence of cirrus, particularly thin cirrus, retrieved AOTs (τ'_{aer}) from ground-based Sun photometry measurements will contain a certain amount of error. Hence, the spectrally dependent AOT (τ_{aer}) can be expressed as

$$\tau'_{\text{aer}}(\lambda) = \tau_{\text{aer}}(\lambda) + \varepsilon(\lambda), \quad (7)$$

where $\varepsilon(\lambda)$ are the effects of clouds, etc. For this study, $\varepsilon(\lambda) = \text{COT}(\lambda)$ at $\lambda = 550\text{ nm}$. Of course, Rayleigh scattering and ozone contributions to the total optical thickness are also important. However, we approximate their contribution relative to that of aerosol as negligible. Following equations (4)–(6), cirrus COT can be determined by

$$\text{COT} = \tau'_{\text{aer}}(\lambda) - \% \text{aerosol} \cdot \tau_{\text{aer}}(\lambda), \quad (8)$$

where the second term can be regarded as an adjusted AOT value.

4. Simulations: Spectral Characteristics of Aerosols and Cirrus

Simulations of spectral fluxes for aerosols/cirrus were conducted to gain further insight into the underlying physics of the measurements and address the detection limits for cirrus. Individual cloud and aerosol components are assessed first, followed by aerosol-cirrus combined scenes.

4.1. Cirrus Scene

A series of experiments were designed to examine the spectral characteristics of cirrus clouds, under the assumption that cloud base altitude, based on NRB profiles, is constrained at 13 km. MODTRAN-provided subvisual and standard cirrus models were used to examine the sensitivity of transmitted spectra with respect to changes in COT ($0.01 < \tau_c < 1.0$) to evaluate the detection limits of cirrus. Note that for subvisual/thin and opaque cirrus, MODTRAN's $4\text{ }\mu\text{m}/64\text{ }\mu\text{m}$ cloud models were employed, respectively. All other cloud parameters (e.g., cloud base altitude) were held constant, and with the exception of one reference aerosol run (BB model—AOT = 0.5), all aerosols were turned off for this experiment. The result of the experiment is presented in Figure 4.

To highlight the spectral responses, the color of the curves progressively varies from dark to light blue as COT decreases. Figure 4a reveals that spectral changes in response to varying COT differ by nearly an order of magnitude. Similar trends in spectral shape were also found when decreasing the geometrical thickness of cirrus

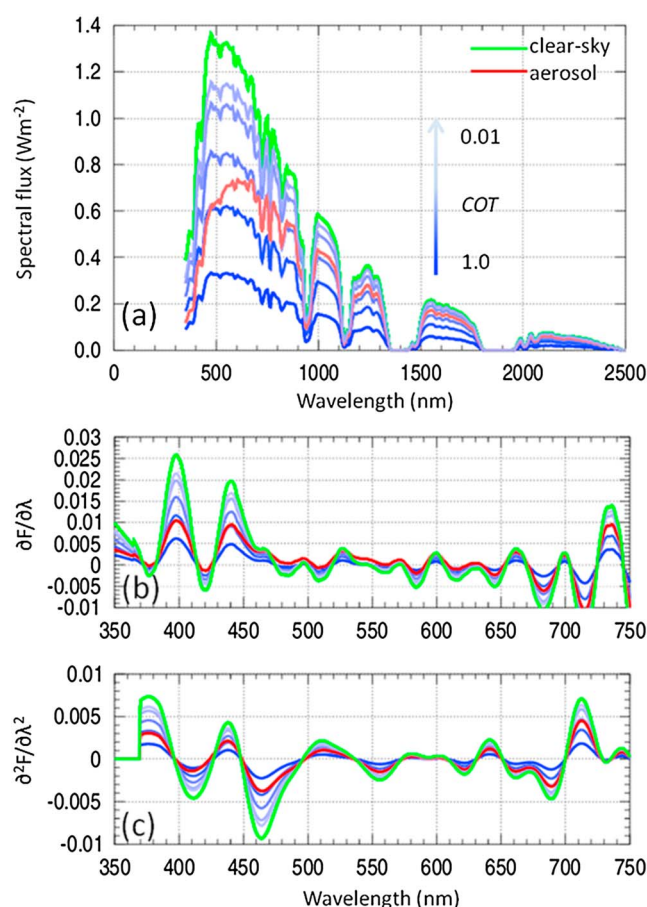


Figure 4. Sensitivity in simulated cirrus spectra (blue curves) for COT using MODTRAN's 4 μm /64 μm ice cloud models compared to (a) clear-sky and aerosol (BB) conditions. Cloud base altitude (H) and thickness (ΔZ) are prescribed to be 13 km and 1 km, respectively. Cloud extinction (km^{-1}) is varied to yield COTs of 0.01, 0.075, 0.25, 0.5, and 1.0. The arrow points in the direction of decreasing COT. All spectra were constrained at 05:00 Coordinated Universal Time (UTC) (12:00 local time) centered at Phimai (15.183°N, 102.565°E). (b and c) First- and second-order spectral derivatives, with the same color code in Figure 4a, are also shown.

changes in aerosol composition and hygroscopic behavior, respectively. The former test includes water-soluble (WS) and -insoluble (WI) components, sulfate (SU), soot (SO), and biomass-burning smoke (BB), and for comparison, an optical model derived from AERONET-retrieved data (3 May) at Phimai (AER). The AER model was based on data (asymmetry parameter and extinction/absorption optical depths) at wavelengths corresponding to the sky radiance measurements (440 nm, 670 nm, 870 nm, and 1020 nm) and then interpolated within MODTRAN across the spectral domain. The latter test evaluates the spectral response to hygroscopic particle growth due to extreme changes in RH (0–90%). To estimate these effects, an empirical formulation of the growth factor from Li *et al.* [2013] is applied to sulfate particles.

The aerosol results are presented in Figure 5. Spectral sensitivity to composition (Figure 5a), assuming dry particles (RH = 0%), reveals a strong dependence on the type of aerosols present and occurs mainly from $\lambda \sim 350$ –750 nm. From the aerosol types examined, a few distinct groups of spectral signatures are evident. Note the similarity in slope between the BB and AER models, compared to that of other aerosols. SU, by comparison, is found to be nearly spectrally flat, whereas SO is momentarily flat with increasing wavelength following a moderate peak and then rapidly decreases with increasing wavelength. WS and WI both peak quickly then steadily decrease with increasing wavelength (note that the WS and WI spectra are similar). Spectral sensitivity is minimal at longer wavelengths (Figure 5b), since these aerosols mostly consist of submicron particles [Li *et al.*, 2013].

from $\Delta Z = 1.0$ –0.25 km (not shown). Clearly, as cirrus clouds become optically thinner, the spectral flux slopes become steeper at the shorter wavelengths ($\lambda < 400$ nm). Evidently, in the limit of increasingly thinner cirrus, the spectral signature approaches that for clear-sky conditions (green curve), where visibility is prescribed at 80 km in the RTM.

The magnitudes of the clear-sky derivative spectra (Figures 4b and 4c) are largest and are set apart from cirrus and aerosol. Across specific spectral bands, particularly between ~ 475 –525 nm and ~ 550 –570 nm, the first derivatives (Figure 4b) for aerosol are of opposite sign to those of clear-sky and cirrus. Also, between ~ 495 and 500 nm, the second derivative spectra (Figure 4c) reveal an approximate 2 nm separation in the inflection points ($\partial^2 F / \partial \lambda^2 = 0$) between cirrus and aerosol spectra. Importantly, the above relationships hold true over the range of COTs tested, including optically thin cases. This suggests that the differences in derivatives can be exploited for separating the media. Based on these differences, a conservative estimate of the lower COT detection limit is ~ 0.03 (thin cirrus regime).

4.2. Aerosol Scene

Similar to cirrus clouds, aerosols are also examined using the same methodology but with two additional tests designed to observe the spectral sensitivity to

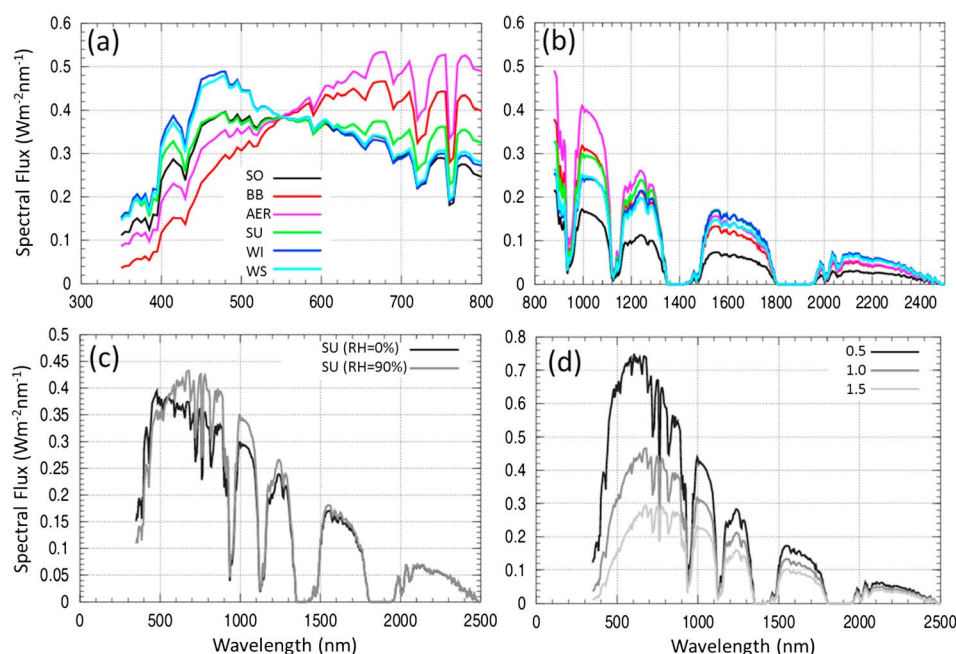


Figure 5. (a) Sensitivity of aerosol composition on spectra for an AOT of 1.0 near solar noon at the short wavelengths. (b) Same as Figure 5a but for the longer wavelengths. Spectra marked BB/AER are most representative of an aerosol mixture. The remaining spectra are the single-aerosol species derived from OPAC: SO, SU, WI, and WS, all evaluated at RH = 0%. (c) Hygroscopic behavior of sulfate from RH = 0% to RH = 90% using an empirical growth factor of 1.6 [Li et al., 2013]. (d) Spectral sensitivity to AOT using the BB model. From top to bottom, AOT (τ) increases in the order of 0.5, 1.0, and 1.5. As AOT increases, the slopes progressively decrease at the shorter wavelengths. See text for details.

Relative to dry particles, growth factors varied between ~ 1.0 and 2.0 for changes in RH in the range of 50–90%, respectively. Aerosol hygroscopic growth in high-RH environments is important, as it can lead to enhancements in scattering [Pan et al., 2009]. Figure 5c shows the change in spectral shape for SU when RH increases from 0 to 90%. Consequently, a change of sign in spectral slope (500–700 nm) for SU is evident (refer to Figure 7), where higher RH causes the slope to become positive.

The dominant spectral response occurred when column AOT was perturbed (Figure 5d). Scaling AOT by a factor of 2–3 times has the effect of significantly decreasing the spectral slopes at the shorter wavelengths. The least sensitive test performed was in changing the aerosol height/thickness (not shown), since aerosols were observed to be mostly constrained in the boundary layer, as corroborated by MPL measurements and which has been found to be a relatively common attribute regionally [Campbell et al., 2013].

4.3. Combined Aerosol and Cirrus Scene

The spectral sensitivity of a cirrus-BB aerosol combined spectrum is presented (shaded orange curves, Figure 6a). Clear-sky (green curve), cirrus (COT = 1: blue curves), and aerosol (red curves) spectra, all calculated at 12:30 P.M. local time, are also shown for reference. For the combined scene, results conclusively show that the signal is unsurprisingly a weighted spectrum of the two-component spectra, which of course is dependent on the cirrus/aerosol model parameters. As AOT increases between 0.25, 0.5, and 1.0 (labeled 1–3, respectively, and the color shading becomes progressively darker), the combined signal transitions from a reasonable cirrus fit to one that becomes more aerosol-like (i.e., better agreement in the shortwave slopes), making it difficult to partition the COT. From an aerosol perspective, this scenario is likely to be optimal anyhow, since cirrus contamination will have a negligible impact on aerosol retrievals. On the other hand, under light to moderate AOT conditions (~ 0.25), the effects of cirrus become more discernible.

In Figure 6b are two sets of curves representing the slopes of aerosols from $\lambda = 500$ –700 nm, as a function of AOT ($\tau = 0.0$ –2.0), combined with two limiting cases of cirrus: thin cirrus ($\tau_c = 0.01$: light color) and thick cirrus ($\tau_c = 1.0$: dark color). The individual curves depict a total of nine aerosol types. Immediately, one can see that

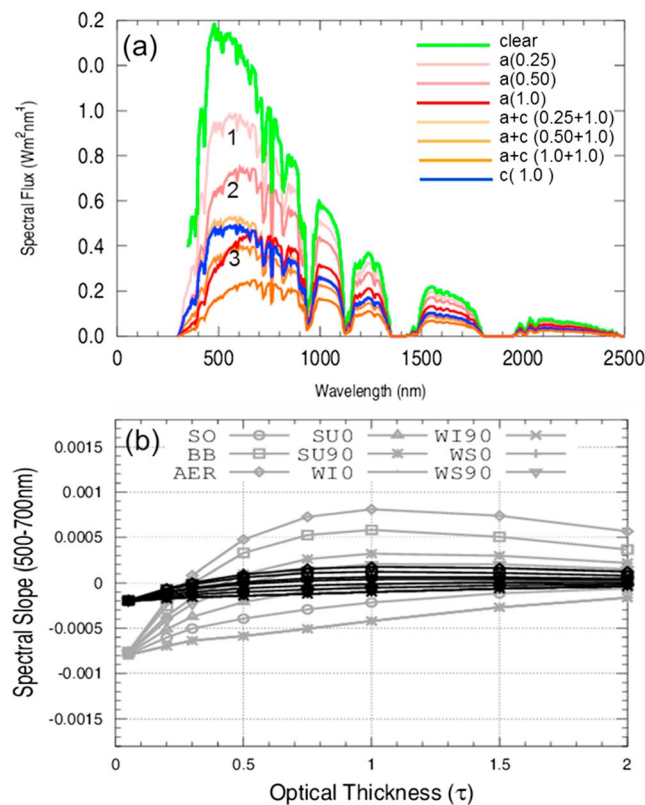


Figure 6. (a) Spectral sensitivity of a combined aerosol (BB)-thin cirrus ($D_{\text{eff}} = 4 \mu\text{m}$) scene, where cirrus height (at cloud base), thickness, and extinction are 13 km, 0.5 km, and 1 km^{-1} , respectively. The shaded red, blue, and shaded orange curves represent (a) aerosol only, (c) cirrus only for $\text{COT} = 1$, and (a + c) aerosol combined with cirrus, respectively. The shaded colors depict the progressive increases in aerosol. Aerosol loading increases from top to bottom, where (1–3) represent the incremental increases in AOT (0.25–0.50–1.0). If loading is light to moderate ($\tau \sim 0.25$), the combined signal adheres closer to the cloud spectrum, otherwise the mismatch becomes more apparent. (b) Spectral slopes of combined aerosol-cirrus scenes from $\lambda = 500\text{--}700 \text{ nm}$. The two groups of curves represent aerosol-thin cirrus (gray: $\text{COT} = 0.01$) and aerosol-thick cirrus (black: $\text{COT} = 1.0$), respectively, with each curve depicting aerosol type. Note the tendency to become spectrally flat as COT increases.

as cirrus becomes optically thicker, the spectral slopes of the transmitted spectra become virtually flat (i.e., they all tend to zero); however, as COT decreases, the effect of aerosols becomes more pronounced, with the slopes deviating from 0 and increasing in magnitude. Generally, across this bandwidth, the tendency is for cirrus to pull the slopes more negative as COT increases and vice versa. Relative to the slope for low background aerosol conditions (-0.0008 at $\text{AOT} = 0.05$) with no cirrus ($\text{COT} = 0$), a perturbation in COT of 0.01 (subvisual regime) introduces a 1% slope increase in the transmitted spectra, which in a noisy background may be difficult to discern. Further perturbations in COT of 0.03–0.3 (thin cirrus regime) have a much larger effect on the relative slopes ($\sim 4\text{--}34\%$, respectively). Finally, for thick cirrus ($\text{COT} = 3.0$), the slopes, as shown, are nearly flat. Interestingly, the BB and AER models were also found to exhibit positive slopes (for $\text{AOT} \geq 0.3$) compared to the negative slopes for thin cirrus and the single-component aerosol species (e.g., sulfate and soot) under dry ($\text{RH} = 0\%$) conditions. The slopes are of opposite sign because the absorption coefficients of the media increase/decrease over this bandwidth. For relatively thin cirrus only, when COT is varied from 0.1 to 1.0 (not shown), the slope remains negative but becomes more positive as COT increases.

To gauge model performance, simulations are compared to ASD spectra for two near-extreme cases identified with MPL and AERONET data: (1) low-aerosol loading ($\text{AOT} \sim 0.16$) under high-level cirrus conditions (3 April at 03:02 UTC) and (2) high-aerosol loading ($\text{AOT} \sim 1.1$) with no detectable cirrus (11 March at 03:20 UTC). It is noted that the averaged MPL-retrieved COT for 3 April (~ 0.02 over lidar ratios 15/30 sr) was used to constrain the model. Figure 7 compares the measured (solid black) and modeled (dashed gray) spectra, respectively, for both cirrus (upper curves) and aerosol (lower curves) cases. Modeled/measured spectral slopes from 500 to 700 nm are given by the gray/black dashed lines, respectively. Note that aerosols/cirrus have slopes that are positive/negative, respectively. For 3 April, a mixed scene consisting of BB aerosol and thin cirrus ($4 \mu\text{m}$ model) was used, while for 11 March, the same BB aerosol model was employed for aerosol-only conditions.

Both models compare reasonably well with the measurements, although the slopes for cirrus/aerosol were found to be slightly smaller/larger than those observed, respectively. At a cirrus COT of 0.03 (within the 1σ level for this study's MPL retrievals—0.04), the cirrus model compares favorably with the measurements having near identical slopes (not shown). Cirrus and aerosol model differences are attributable to the much larger compositional parameter space of aerosols over ice.

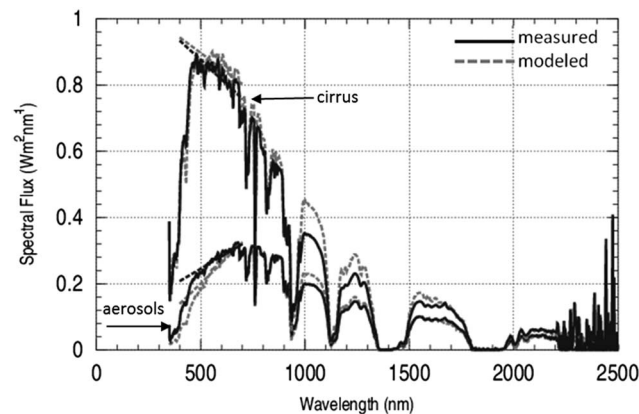


Figure 7. Model versus measured spectra for cirrus (top curves) and aerosol (bottom spectra) for two extreme cases. See text for details. The black/gray dotted lines denote the slopes for the measured/modeled spectra, respectively, from $\lambda = 500$ – 700 nm. Noise in the measurements is evident from $\sim\lambda = 2200$ – 2500 .

5. Aerosol-Cirrus Test Cases

To illustrate the utility of the spectral derivative technique, several cases of combined aerosol-cirrus scenes from BASE-ASIA were selected using the AERONET Level 2 AOTs, MPL NRB profiles, and retrieved cloud data from the MPL cloud detection algorithm. COTs from the MODIS MOD6 cloud product were also used and served as a source of independent, initial constraints for the RTM's cloud layer extinction. Note that COTs retrieved from the MPL cloud detection algorithm provided a benchmark for comparing the results in this study (section 6).

Pertinent MPL-retrieved data included cloud base / cloud top altitudes and COT

for each detected layer and total COT across all layers. The algorithm uses a combination of two methods to identify cloud boundaries from the Level 1 NRB profile [Campbell *et al.*, 2008; Lewis *et al.*, manuscript in preparation, 2014]. The first method requires the first derivative of the lidar signal to exceed a minimum threshold in order to detect a cloud layer. The assumption of a strong gradient in the signal makes this first method best suited for low liquid-water phase clouds [e.g., Clothiaux *et al.*, 1998] and is referred to as the gradient-based cloud detection method (GCDM). The second method is designed for use in cases of weak SNR and relies on uncertainties in the lidar signal. This method is primarily used to detect high clouds and is referred to as the uncertainty-based cloud detection method (UCDM).

The cloud retrievals for this study are made using the UCDM. However, the GCDM is used to screen clouds below 5 km whenever possible, in order to ensure that we have a relatively unobstructed view of the upper troposphere, and thus optimal SNR for the UCDM. A 30 min rolling average is used for the cloud retrievals in order to decrease noise from the solar background. Chew *et al.* [2011] showed that uncertainties in the parameterized lidar ratio largely contribute to uncertainties in the MPL-retrieved COT (a research-level data product). For example, the authors showed that using a lidar ratio of 15/25 sr can lead to a mean-estimated COT contamination of 0.067/0.12, respectively, in the Level 2 AERONET AOT at Singapore. The current study used lidar ratios of 15 and 30 sr to cover a representative range given in the literature [e.g., Winker *et al.*, 2009; Chew *et al.*, 2011]. This range is designed to account for presumed variances of optical properties for different cirrus clouds observed at Phimai (e.g., upper tropospheric convective outflow).

MODIS cloud data were obtained from NASA/Goddard Space Flight Center's MOD06_L2 Collection 051 Terra product files [Platnick *et al.*, 2003] over the domain of interest from 26 February to 5 May 2006. The domain is defined as a square box centered at Phimai (15.183°N, 102.565°E) extending 0.2° (~ 22 km) in each direction. Statistics are computed for COT/CTP at all times available during the scan. Six optimal test cases were identified (Table 3), where cirrus coexisted with aerosols (confirmed by AERONET observations) and were relatively high level (>10 km) and perceptibly thin (i.e., cloud geometrical thickness) based on the MPL NRB profiles (Figure 8). Cirrus cloud base altitudes (H) are mostly ~ 11 – 15 km with a thickness (ΔZ) of ≤ 1 km. One exception is on 20 April, which clearly reveals multilayered cirrus at the time of the MODIS overpass (solid white line). Corresponding total sky (i.e., hemispherical) images (not shown) for these cases reveal streaks of cirrus that are barely discernible. For reference, a total sky image for 23 March is shown in Figure 4 of Huang *et al.* [2011].

Aerosols, on the other hand, are clearly evident in the PBL. Near-coincident ground-based Level 2 AOTs from the AERONET Sun photometer were found within ± 30 min of the MODIS overpass. The Dashed and solid white lines mark the MODIS overpass time plus ± 30 min, respectively, during which AERONET retrievals were found. Clearly, the cloud screen algorithm [Smirnov *et al.*, 2000] removed all of the cirrus data points on 12 April (i.e., there are no dashed lines). However, for 12 and 23 March, the cirrus data were missed (Level 1 and 2 processed data were equivalent) about the overpass time. Note the proximity of the dashed lines. It is plausible that the cirrus layers for these two cases were relatively heterogeneous during the Sun photometer's measurement

Table 3. MOD06 Cloud Statistics for Cirrus Cases

Cirrus Cases	Cloud Parameters	MOD06 Cloud Statistics					
		Median	Mean	Standard	Min	Max	Sample Size ^a Deviation (1 σ)
03/12 ^b	COT	0.79	0.75	0.32	0.02	1.71	257
(03:25 UTC)	CTP	367.5	503.5	284.8	200.0	1015.0	122
03/23 ^b	COT	1.08	1.09	0.43	0.01	4.03	745
(03:10 UTC)	CTP	210.0	348.6	296.7	140.0	985.0	52
04/12	COT	0.72	0.75	0.39	0.01	1.82	160
(04:30 UTC)	CTP	235.0	239.72	25.27	200.0	300.0	36
04/20	COT	2.46	3.07	1.51	1.22	14.01	1750
(03:35 UTC)	CTP	200.0	202.5	19.03	160.0	245.0	72
04/22	COT	0.91	0.95	0.496	0.01	2.7	678
(03:20 UTC)	CTP	337.5	578.8	362.4	200.0	1015.0	78
05/03	COT	0.98	0.917	0.317	0.04	3.02	419
(03:05 UTC)	CTP	285.0	411.9	294.4	180.0	985.0	26

^aDifferences in COT/CTP sample sizes are due to differences in resolution: 1 km for COT and 5 km for CTP.

^bCirrus clouds not detected in AERONET L2 processing.

period (i.e., triplet stability and smoothness criteria both passed) and consequently were not screened. A comparison of the Level 1 and 2 data revealed that cirrus data points were also removed for 20 April, 22 April, and 3 May. Thus, the cloud algorithm was effective for the majority of cases.

6. Results and Uncertainties

Following the methodology in section 3, cirrus COTs were derived for a total of 10 aerosol/cirrus model combinations over the six cases examined. On average, the weights (w) that describe the percentage

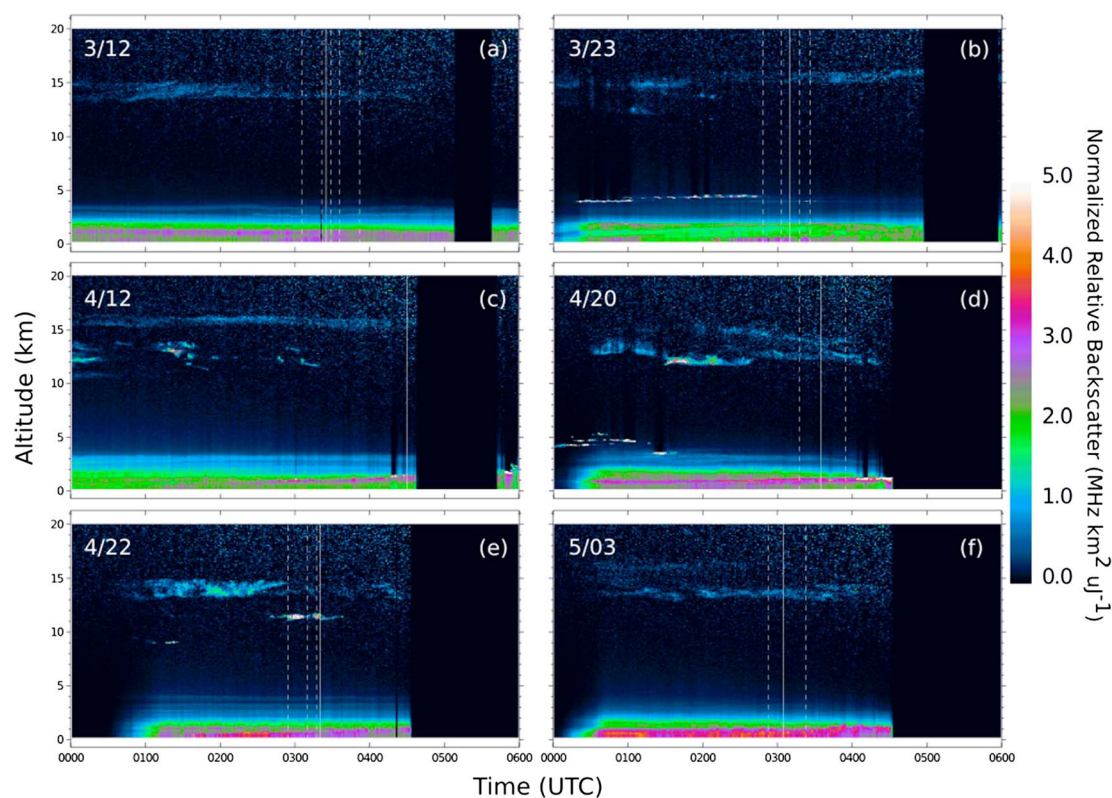


Figure 8. (a–f) MPL NRB profiles (in $\text{MHz km}^2 \mu\text{J}^{-1}$) for selected aerosol-cirrus cases during BASE-ASIA. The darkened regions along right-hand side of each plot denote the times near solar noon when the MPL was shaded to preclude damage to the fore optic. The solid/dashed white lines mark the locations of the satellite overpass and nearest AERONET retrieval times (satellite overpass ± 30 min), respectively. Note that on 12 April, there were no AERONET retrievals around the satellite overpass due to cloud screening. See text for details.

Table 4. Partitioning Cirrus and Aerosol Optical Thickness

Table 4. Partitioning Cirrus and Aerosol Optical Thickness																	
AERONET AOT			Cirrus COT (Aerosol Models)														
Cirrus Cases	L1	L2	Aerosol Weight ^a	Cloud Weight ^a	SO 4 ^b	SO 10 ^c	BB ^d	AER ^e	SU 0 ^f	SU 90 ^g	WI 0 ^h	WI 90 ⁱ	WS 0 ^j	WS 90 ^k	Average COT ^a	Adjusted AOT ^a	
03/12 ^l (03:25 UTC)	0.69	0.69	0.87	0.13	0.05	0.05	0.03	0.03	0.03	0.03	0.20	0.17	0.21	0.03	0.09 ± 0.07	0.60	
03/23 ^l (03:10 UTC)	0.34	0.34	0.85	0.15	0.05	0.02	0.05	0.03	0.04	0.03	0.06	0.05	0.06	0.05	0.05 ± 0.01	0.29	
04/12 (04:20 UTC)	0.39	0.34	0.86	0.14	0.07	0.02	0.05	0.04	0.03	0.04	0.04	0.04	0.04	0.04	0.04 ± 0.01	0.35	
04/20 (03:35 UTC)	0.87	0.86	0.78	0.22	0.09	0.11	0.11	0.16	0.21	0.09	0.33	0.28	0.33	0.11	0.18 ± 0.09	0.67	
04/22 (03:20 UTC)	0.39	0.29	0.86	0.14	0.04	0.02	0.04	0.03	0.04	0.03	0.04	0.04	0.04	0.04	0.04 ± 0.01	0.35	
05/03 (03:05 UTC)	0.51	0.51	0.79	0.21	0.07	0.07	0.11	0.10	0.11	0.08	0.15	0.11	0.15	0.08	0.10 ± 0.03	0.41	
Case averages	0.53	0.51	0.83	0.17	0.06	0.05	0.07	0.07	0.08	0.05	0.14	0.12	0.14	0.06	0.08 ± 0.03	0.44	
^a Averaged quantities.																	
^b SO4: Soot + 4 μm cirrus model.																	
^c SO10: Soot + 10 μm cirrus model.																	
^d BB: Biomass-burning smoke model [Carr, 2005].																	
^e AER: AERONET model at Phimai.																	
^f SU0: Sulfate (RH = 0%).																	
^g SU90: Sulfate (RH = 90%).																	
^h WI0: Water Insoluble (RH = 0%).																	
ⁱ WI90: Water Insoluble (RH = 90%).																	
^j WS0: Water soluble (RH = 0%).																	
^k WS90: Water soluble (RH = 90%).																	
^l Cirrus not detected in AERONET L2 processing.																	

^aAveraged quantities.^bSO4: Soot + 4 μm cirrus model.^cSO10: Soot + 10 μm cirrus model.^dBB: Biomass-burning smoke model [Carr, 2005].^eAER: AERONET model at Phimai.^fSU0: Sulfate (RH = 0%).^gSU90: Sulfate (RH = 90%).^hWI0: Water Insoluble (RH = 0%).ⁱWI90: Water Insoluble (RH = 90%).^jWS0: Water soluble (RH = 0%).^kWS90: Water soluble (RH = 90%).^lCirrus not detected in AERONET L2 processing.

variability in the measured spectra at Phimai due to aerosols and cirrus were found to be ~83% and 17%, respectively. Consequently, the mean ($\pm 1\sigma$) cirrus COT over all models evaluated was $\sim 0.08 \pm 0.03$. Results are summarized in Table 4. The columns from left to right depict the cirrus cases, the AERONET Level 1 and 2 retrieved AOTs, the corresponding weights (w) for aerosols and cirrus (equations (4)–(6)), the derived COTs (equation (9)) for each aerosol model and their averaged values ($\pm 1\sigma$), and lastly the adjusted AOTs (average $\pm 1\sigma$) (equation (9)). Coincident with the MODIS overpass times (± 1 min), derived COTs ranged from as low as 0.02 to as high as 0.33 with minimum/maximum values occurring on 22 April and 20 April, respectively. The higher COTs on 20 April are likely due to the presence of multilayered cirrus clouds (Figure 8), which seem to exhibit more complex structure. This is consistent with the maximum MOD06 COT value in Table 3 for 20 April (2.46), albeit is much larger by nearly an order of magnitude, which may be attributed to the inherent difficulties in retrieving multilayered cirrus from space [Marchand *et al.*, 2010]. The lowest COTs were found for 23 March, similar to that reported by Huang *et al.* [2011], along with 12 and 22 April.

Next, this study's COTs are compared with those derived from the MPL cloud retrieval algorithm for each lidar ratio (Figure 9). Errors bars denoting the $\pm 1\sigma$ in the data are indicated. Within the 1σ range, the COTs over all the six cases compare relatively well, with the averaged MPL (lidar ratios 15/30 sr) and ASD data being 0.09 ± 0.04 and 0.08 ± 0.03 , respectively. Given the differences in viewing geometry of both instruments (MPL is a zenith-viewing instrument whereas the ASD tracks the Sun), these comparisons are reasonable, yielding confidence in the methodology.

Figure 10 depicts the COTs (Figure 10a), the aerosol weighting coefficients (Figure 10b), and the cirrus weighting

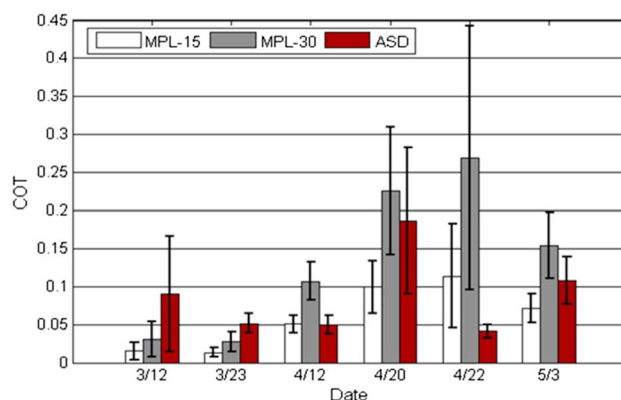


Figure 9. Comparisons between the MPL and ASD COTs for each cirrus case. MPL COTs are shown for lidar ratios 15 and 30 sr, for consistency with literature, and to account for the variable cirrus clouds at Phimai (section 5). The error bars denote the ± 1 standard deviation.

the WS (RH = 90%) aerosols. The aerosol weights for the WI and WS (RH = 0%) models were significantly lower than the others, perhaps implying that during the experiment, (1) the crustal aerosols were not dominant and (2) the RH was much higher. For SO, the combined 10 μm thin cirrus model (SO10) achieved a better fit with the data than did the 4 μm thin cirrus model (SO4), suggesting a larger effective particle size.

Additionally, it was found that if the model's column water vapor amount is gradually reduced with all other parameters held constant, this has the effect of increasing the COT. This is because as the troposphere becomes drier, scattering photons from cirrus clouds—which normally would get absorbed by atmospheric water vapor—are now able to travel over longer path lengths unaffected by the drier layers. For example, reducing precipitable water vapor in the model's standard tropical atmosphere by $\sim 50\%$ nearly doubles the COT (~ 0.003 to 0.005).

For the cases studied, AERONET-retrieved L2 AOTs ranged from 0.29 to 0.86 (Table 4). Note that the AERONET L2 values were interpolated to the closest MODIS overpass times (Table 3). Consequently, for 3 May, the L2 and L1 values are shown to be equal even though the cloud screen algorithm did effectively remove cirrus. Further evaluation of both L1 and L2 data sets revealed that for two cases (12 and 23 March—marked by the single asterisk), the cloud screening algorithm did not detect cirrus. It is plausible that the cirrus layers for these two cases were relatively stable and uniform during the Sun photometer's measurement period.

Primary sources of uncertainty in the derived cirrus COTs are mainly attributable to the modeled aerosol/cloud properties, particularly aerosol composition and the MODIS MOD06 and AERONET-retrieved parameters. Temporal offsets between ASD and MODIS observations can also add uncertainty to the derived COTs. To minimize these effects, all spectral measurements, except for 12 April, are within ± 1 min of the MODIS overpass. For 12 April, the closest temporal match was within 9 min due to the unavailability of the ASD data. Temporal offsets are related to changes in the Sun's position and atmospheric conditions which can alter the spectral profile. Additional uncertainties also stem from the choice of smoothing parameters (i.e., filter width and order of the polynomial fit), as well as bandwidth $\Delta\lambda$ over which the derivative approximation is computed (section 3). Future work will investigate the effects of the smoothing parameters and bandwidth $\Delta\lambda$ in further detail. Standard uncertainties in COT are defined as the 1σ standard deviation divided by the mean for each source x including aerosol model, MODIS MOD06 cloud properties, and AERONET retrieved AOTs. The aerosol uncertainties are weighted with the values obtained in the absolute solution (Figure 10b). The combined uncertainty is computed as

$$\text{root-sum-square} = \sqrt{(x_1)^2 + (x_2)^2 + \dots + (x_n)^2}, \quad (9)$$

by taking the root sum of the square of all sources (i.e., summation in quadrature), assuming that they are independent from each other. Considering all the six cases, the total uncertainty was found to be $\sim 57\%$ with

coefficients (Figure 10c) as functions of both aerosol model and cirrus case. Note that the data were interpolated to help visualize the differences between the cases and models examined. Data values lie along the grid lines, whereas points off the grid do not bear any physical meaning. The COTs for each case are shown in Figure 10a with the lowest days being 23 March and 12 and 22 April. The sum of the weighting coefficients in Figures 10b and 10c should be equal to 1, where the influence of cirrus is balanced by the larger aerosol contributions. The aerosol models that best fit the measured data at Phimai ($\geq 85\%$: bright areas in Figure 10b) for most cases were SO, SU (RH = 90%), and

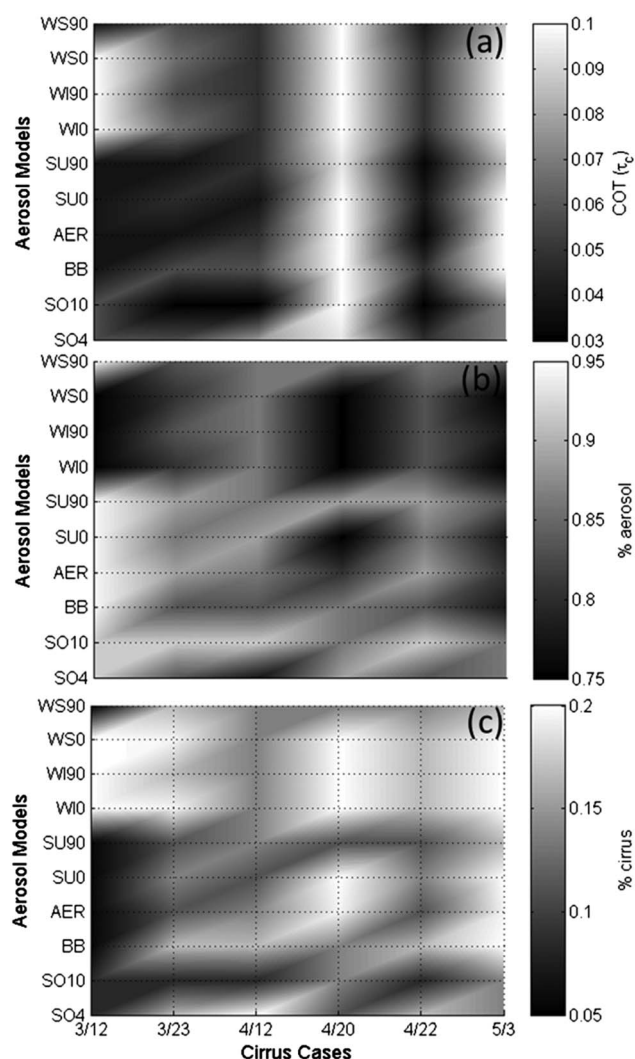


Figure 10. Parameter distributions over all the cirrus cases and aerosol models examined for (a) partitioned cirrus COTs, (b) aerosol weighting coefficients, and (c) cirrus weighting coefficients. The vertical/horizontal axes denote the aerosol models and cirrus cases, respectively. The bright/dark colors denote the high/low COTs and weighting coefficients, respectively. See section 6 for details.

can be discerned from aerosols on the basis of their derivative spectra. Model simulations also reveal that the broader 500–700 nm band yields valuable information for separating atmospheric components. For mixed aerosol (BB smoke and AERONET models)/cirrus only cases, spectral slopes were positive/negative respectively. The slopes are of opposite sign because the media's absorption coefficients increase/decrease across this band. In dry conditions, negative slopes were identified for sulfate/water-soluble species; however,

aerosol composition being the largest (~59%), hence the importance of the aerosol model. If the multilayer cirrus case (20 April) is not considered, the total uncertainty was found to be ~48% with aerosol composition being the largest (~45%). A summary of these results is presented in Table 5.

7. Conclusions

Derivative spectroscopy was applied to hyperspectral, ground-based solar measurements during the 2006 BASE-ASIA field experiment to study aerosols and cirrus clouds. A finite difference approximation was used to compute the first two derivatives of measured/modeled transmitted spectral fluxes. The informational content of the media is encoded in the shapes, magnitudes, and positions of the resulting spectral peaks, mostly from $\lambda = 350\text{--}750\text{ nm}$, which are often obscured in the original signals. Across subbands of this region, aerosol and cloud spectra exhibit opposite slopes (~475–525 nm and ~550–570 nm) and display subtle changes in their curvature ($\lambda \sim 500\text{ nm}$), where values of the second derivative shift from concave up to concave down and vice versa.

In general, cirrus spectra were found to be relatively flat, whereas aerosol spectra display many marked features, owing to the diverse chemical composition of aerosols over ice. In the optically thin limit (COT ~0.03), sensitivity experiments show cirrus

can be discerned from aerosols on the basis of their derivative spectra. Model simulations also reveal that the broader 500–700 nm band yields valuable information for separating atmospheric components. For mixed aerosol (BB smoke and AERONET models)/cirrus only cases, spectral slopes were positive/negative respectively. The slopes are of opposite sign because the media's absorption coefficients increase/decrease across this band. In dry conditions, negative slopes were identified for sulfate/water-soluble species; however, in moist environments, the slopes become positive. When COT increases for combined aerosol-cirrus scenes, the slopes of the transmitted spectra become nearly flat. However, as COT decreases, the effect of aerosols becomes more pronounced, with the slopes increasing in magnitude. In mixed scenes, the tendency is for cirrus to pull the

Table 5. COT-Estimated Uncertainties

Source	Uncertainty	Comments
Aerosol models ^a	57%	computed over 10 models
MOD06 COTs	16%	± 1 standard deviation about the mean
AERONET AOT	1%	± 0.01 at $\tau = 0.50$
Combined	59%	over all cases

^aDerived COTs for each model multiplied by their respective weighted solutions (Figure 10b).

slopes more negative as COT increases and vice versa. Derivative spectra of the aerosol models reveal distinct differences in their spectral signatures which can be useful for developing aerosol classification schemes.

To illustrate the efficacy of this approach, first-/second-order derivative spectra were employed in a best two model fit to determine the relative weightings of aerosols/cirrus in the observations. Consequently, cirrus COT can be partitioned from retrieved AOT measurements. The technique was applied to selected high-altitude cirrus cases, coincident with collocated ASD, MPLNET, and AERONET measurements during BASE-ASIA 2006. The mean ($\pm 1\sigma$) cirrus COT was found to be $\sim 0.08 \pm 0.03$ which compared reasonably well with the averaged MPL-retrieved values (0.09 ± 0.04 over lidar ratios 15/30 sr). Consistent with previous studies, the measured spectra were mainly dominated by soot, sulfate, and water-soluble components. Estimated uncertainties in the derived COTs for this study were found to be dominated by aerosol composition (57%) with a combined uncertainty of 59%. Ongoing work will continue investigating (1) the application of higher-order derivatives in hyperspectral data analysis and (2) the relationships between aerosol/cloud properties (e.g., particle size, shape, refractive index, and mixtures) and derivative order. Future work will build from current results to (1) develop aerosol spectral classification schemes and (2) advance a more robust aerosol-cirrus detection algorithm to study, for example, cirrus properties and contamination effects on aerosol retrievals. Undoubtedly, derivative analysis is a versatile tool that can be exploited for studying the fine optical structure of atmospheric media in high-resolution, remote sensing data.

Acknowledgments

This work is supported by the NASA Radiation Sciences Program managed by Hal B. Maring. Both AERONET and MPLNET are funded by the NASA Earth Observing System and Radiation Sciences Program. We would like to thank B. Holben for establishing and maintaining the AERONET site at Phimai and for the valuable discussions. We acknowledge the MODTRAN developers (a joint collaboration of Spectral Sciences, Inc. and the U.S. Air Force) for their RTM code and M. Hess for making the OPAC database publicly available. We would like to thank G. Fager at PANalytical NIR (formerly ASD) for his technical support of our FieldSpec Pro instrument and D. Feldman and T. O'Haven for their MODTRAN wrapper and signal-processing codes (terpconnect.umd.edu/~toh/spectrum/SignalProcessingTools.html), respectively. We also thank B. Baum, P. Yang, A. Heymsfield, and C. Schmitt for their ice cloud scattering models. Lastly, we thank the reviewers for their helpful and insightful comments.

References

- Anderson, G. P., S. A. Clough, F. X. Kneizys, J. H. Chetwynd, and E. P. Shettle (1986), AFGL atmospheric constituent profiles (0–120 km), *Tech. Rep. AFGL-TR-86-0110*, Environ. Res. Pap. 954.
- Anderson, G. P., A. Berk, P. K. Acharya, L. S. Bernstein, S. M. Adler-Golden, J. Lee, and L. Muratov (2009), Reformulated atmospheric band model method for modeling atmospheric propagation at arbitrarily fine spectral resolution and expanded capabilities, U.S. Patent [7593835], issued 22 Sept.
- Bassani, C., V. Estéles, M. Campanelli, R. M. Cavalli, and J. A. Martínez-Lozano (2009), Performance of a FieldSpec spectroradiometer for aerosol optical thickness retrieval: Method and preliminary results, *Appl. Opt.*, 48(11), 1969–1978, doi:10.1364/AO.48.001969.
- Baum, B. A., P. Yang, A. J. Heymsfield, C. Schmitt, Y. Xie, A. Bansemir, Y. X. Hu, and Z. Zhang (2011), Improvements to shortwave bulk scattering and absorption models for the remote sensing of ice clouds, *J. Appl. Meteorol. Climatol.*, 50, 1037–1056, doi:10.1175/2010JAMC2608.1.
- Bellisola G., and C. Sorio (2012), Infrared spectroscopy and microscopy in cancer research and diagnosis, *Am. J. Cancer Res.*, 2(1), 1–21.
- Berk, A., et al. (2006), MODTRAN5: 2006 update, *Proc. SPIE*, 6233, 62331 F.
- Berk, A., P. K. Acharya, L. S. Bernstein, G. P. Anderson, P. Lewis, J. H. Chetwynd, and M. L. Hoke (2008), Band model method for modeling atmospheric propagation at arbitrarily fine spectral resolution, U.S. Patent [7433806], issued 7 Oct.
- Butler, W. L., and D. W. Hopkins (1970), An analysis of fourth derivative spectra, *Photochem. Photobiol.*, 12, 451–456, doi:10.1111/j.1751-1097.1970.tb06077.x.
- Campbell, J. R., K. Sassen, and E. J. Welton (2008), Elevated cloud and aerosol layer retrievals from micropulse lidar signal profiles, *J. Atmos. Oceanic Technol.*, 25, 685–700, doi:10.1175/2007JTECHA1034.1.
- Campbell, J. R., J. S. Reid, D. L. Westphal, J. Zhang, J. L. Tackett, B. N. Chew, E. J. Welton, A. Shimizu, N. Sugimoto, and K. Aoki (2013), Characterizing the vertical profile of aerosol particle extinction and linear depolarization over Southeast Asia and the Maritime Continent: The 2007–2009 view from CALIOP, *Atmos. Res.*, 122, 520–543, doi:10.1016/j.atmosres.2012.05.007.
- Carr, S. B. (2005), The aerosol models in MODTRAN: Incorporating selected measurements from northern Australia, *Tech. Rep. DSTO-TR-1803*, Defence Science and Technology Organisation, Edinburgh, South Australia, Australia.
- Chew, B., J. Campbell, J. Reid, D. Giles, E. Welton, S. Salinas, and S. Liew (2011), Tropical cirrus cloud contamination in sun photometer data, *Atmos. Environ.*, 45, 6724–6731, doi:10.1016/j.atmosenv.2011.08.017.
- Clevers, J. G. P. W., L. Kooistra, and M. E. Schaepman (2010), Estimating canopy water content using hyperspectral remote sensing data, *Int. J. Appl. Earth Obs. Geoinf.*, 12, 119–125, doi:10.1016/j.jag.2010.01.007.
- Clothiaux, E. E., G. G. Mace, T. P. Ackerman, T. J. Kane, J. D. Spinhirne, and V. S. Scott (1998), An automated algorithm for detection of hydrometeor returns in micropulse lidar data, *J. Atmos. Oceanic Technol.*, 15, 1035–1042, doi:10.1175/1520-0426(1998)015.
- Estep, L., and G. A. Carter (2005), Derivative analysis of AVIRIS data for crop stress detection, *Photogramm. Eng. Remote Sens.*, 71, 1417–1421.
- French, A. N., J. M. Norman, and M. C. Anderson (2003), A simple and fast atmospheric correction for spaceborne remote sensing of surface temperature, *Remote Sens. Environ.*, 87, 326–333, doi:10.1016/j.rse.2003.08.001.
- Guo, G., Q. Ji, P. Yang, and S.-C. Tsay (2005), Remote sensing of cirrus optical and microphysical properties from ground-based infrared radiometric measurements-Part II: Retrievals from CRYSTAL-FACE measurements, *IEEE Geosci. Remote Sens. Lett.*, 2, 132–1351, doi:10.1109/LGRS.2005.844734.
- Hansell, R., et al. (2010), An assessment of the surface longwave direct radiative effect of airborne Saharan dust during the NAMMA field campaign, *J. Atmos. Sci.*, 67, 1048–1065, doi:10.1175/2009JAS3257.1.
- Hansell, R. A., K. N. Liou, S. C. Ou, S. C. Tsay, Q. Ji, and J. S. Reid (2008), Remote sensing of mineral dust aerosol using AERI during the UAE²: A modeling and sensitivity study, *J. Geophys. Res.*, 113, D18202, doi:10.1029/2008JD010246.
- Hansell, R. A., et al. (2012), An assessment of the surface longwave direct radiative effect of airborne dust in Zhangye, China, during the Asian Monsoon Years field experiment (2008), *J. Geophys. Res.*, 117, D00K39, doi:10.1029/2011JD017370.
- Hess, M., P. Koepke, and I. Schult (1998), Optical properties of aerosols and clouds: The software package OPAC, *Bull. Am. Meteorol. Soc.*, 79, 831–844, doi:10.1175/1520-0477(1998)079.
- Heymsfield, A. J., and L. J. Jahnsen (1974), Microstructure of tropopause cirrus layers, paper presented at Sixth Conference on Aerospace and Aeronautical Meteorology, Am. Meteorol. Soc., El Paso, Tex.

- Holben, B. N., et al. (1998), AERONET—A federated instrument network and data archive for aerosol characterization, *Remote Sens. Environ.*, **66**, 1–16, doi:10.1016/S0034-4257(98)00031-5.
- Hsu, N. C., J. R. Herman, and S.-C. Tsay (2003), Radiative impacts from biomass burning in the presence of clouds during boreal spring in Southeast Asia, *Geophys. Res. Lett.*, **30**(5), 1224, doi:10.1029/2002GL016485.
- Huang, J., N. C. Hsu, S.-C. Tsay, M.-J. Jeong, B. N. Holben, T. A. Berkoff, and E. J. Welton (2011), Susceptibility of aerosol optical thickness retrievals to thin cirrus contamination during the BASE-ASIA campaign, *J. Geophys. Res.*, **116**, D08214, doi:10.1029/2010JD014910.
- Huang, J., et al. (2012), Evaluations of cirrus contamination and screening in ground aerosol observations using collocated lidar systems, *J. Geophys. Res.*, **117**, D15204, doi:10.1029/2012JD017757.
- Huang, J., N. C. Hsu, S.-C. Tsay, Z. Liu, M.-J. Jeong, R. A. Hansell, and J. Lee (2013), Use of spaceborne lidar for the evaluation of thin cirrus contamination and screening in the Aqua MODIS Collection 5 aerosol products, *J. Geophys. Res. Atmos.*, **118**, 6444–6453, doi:10.1002/jgrd.50504.
- Hyer, E. J., J. S. Reid, C. Schmidt, L. Giglio, and J. Hoffman (2013), Different views of fire activity over Indonesia and Malaysia from polar and geostationary satellite observations, *Atmos. Res.*, **122**, 504–519, doi:10.1016/j.atmosres.2012.06.011.
- Ji, Q., S.-C. Tsay, K. M. Lau, R. A. Hansell, J. J. Butler, and J. W. Cooper (2011), A novel nonintrusive method to resolve the thermal dome effect of pyrrometers: Radiometric calibration and implications, *J. Geophys. Res.*, **116**, D24105, doi:10.1029/2011JD016466.
- Kim Oanh, N. T., et al. (2006), Particulate air pollution in six Asian cities: Spatial and temporal distributions, and associated sources, *Atmos. Environ.*, **40**, doi:10.1016/j.atmosenv.2006.01.050.
- Kindel, B. C., Z. Qu, and A. F. H. Goetz (2001), Direct solar spectral flux and transmittance measurements from 350 to 2500 nm, *Appl. Opt.*, **40**, 3483–3494.
- Li, C., et al. (2013), Characteristics and composition of atmospheric aerosols in Phimai, Central Thailand during BASE-ASIA, *Atmos. Environ.*, doi:10.1016/j.atmosenv.2012.04.003.
- Lin, N. H., et al. (2013), An overview of regional experiments on biomass burning aerosols and related pollutants in Southeast Asia: From BASE-ASIA and the Dongsha experiment to 7-SEAS, *Atmos. Environ.*, **78**, 1–19, doi:10.1016/j.atmosenv.2013.04.066.
- Lin, N., A. M. Sayer, S.-H. Wang, A. M. Loftus, T.-C. Hsiao, G. R. Sheu, N. C. Hsu, and S.-C. Tsay (2014), Interactions between biomass-burning aerosols and clouds over Southeast Asia: Current status, challenges, and perspectives, *Environ. Pollut.*, in press.
- Marchand, R., T. Ackerman, M. Smyth, and W. B. Rossow (2010), A review of cloud top height and optical depth histograms from MISR, ISCCP, and MODIS, *J. Geophys. Res.*, **115**, D16206, doi:10.1029/2009JD013422.
- McBride, P. J., K. S. Schmidt, P. Pilewskie, A. S. Kittelman, and D. E. Wolfe (2011), A spectral method for retrieving cloud optical thickness and effective radius from surface-based transmittance measurements, *Atmos. Chem. Phys.*, **11**, 7235–7252, doi:10.5194/acp-11-7235-2011.
- McFarquhar, G. M., A. J. Heymsfield, J. Spinhirne, and B. Hart (2000), Thin and subvisual tropopause tropical cirrus: Observations and radiative impacts, *J. Atmos. Sci.*, **57**, 1841–1853, doi:10.1175/1520-0469(2000)057.
- O'Haver, T. C., and G. L. Green (1976), Numerical error analysis of derivative spectroscopy for the quantitative analysis of mixtures, *Anal. Chem.*, **48**, 312, doi:10.1021/ac60366a016.
- O'Neill, N. T., T. F. Eck, A. Smirnov, B. N. Holben, and S. Thulasiraman (2003), Spectral discrimination of coarse and fine mode optical depth, *J. Geophys. Res.*, **108**(D17), 4559, doi:10.1029/2002JD002975.
- Pan, X. L., P. Yan, J. Tang, J. Z. Ma, Z. F. Wang, A. Gbaguidi, and Y. L. Sun (2009), Observational study of influence of aerosol hygroscopic growth on scattering coefficient over rural area near Beijing mega-city, *Atmos. Chem. Phys.*, **9**, 7519–7530, doi:10.5194/acp-9-7519-2009.
- Pilewskie, P., J. Pommier, R. Bergstrom, W. Gore, S. Howard, M. Rabbette, B. Schmid, P. V. Hobbs, and S. C. Tsay (2003), Solar spectral radiative forcing during the Southern African Regional Science Initiative, *J. Geophys. Res.*, **108**(D13), 8486, doi:10.1029/2002JD002411.
- Philpot, W. D. (1991), The derivative ratio algorithm: Avoiding atmospheric effects in remote sensing, *IEEE Trans. Geosci. Remote Sens.*, **29**(3), 350–357, doi:10.1109/36.79425.
- Platnick, S., M. D. King, S. A. Ackerman, W. P. Menzel, B. A. Baum, J. C. Riédi, and R. A. Frey (2003), The MODIS cloud products: Algorithms and examples from Terra, *IEEE Trans. Geosci. Remote Sens.*, **41**, 459–473, doi:10.1109/TGRS.2002.808301.
- Rabbette, M., and P. Pilewskie (2002), Principal component analysis of Arctic solar flux spectra, *J. Geophys. Res.*, **107**(C10), 8049, doi:10.1029/2000JC000566.
- Rothman L.S., et al. (2009), The HITRAN 2008 molecular spectroscopic database, *J. Quant. Spectrosc. Radiat. Transfer*, **110**, 533–572, doi:10.1016/j.jqsrt.2009.02.013.
- Sahu, L. K., Y. Kondo, Y. Miyazaki, P. Pongkiatkul, and N. T. Kim Oanh (2011), Seasonal and diurnal variations of black carbon and organic carbon aerosols in Bangkok, *J. Geophys. Res.*, **116**, D15302, doi:10.1029/2010JD015563.
- Sassen, K., and B. S. Cho (1992), Subvisual-Thin Cirrus Lidar Dataset for Satellite Verification and Climatological Research, *J. Appl. Meteorol.*, **31**, 1275–1285, doi:10.1175/1520-0450(1992)031.
- Savitzky, A., and M. J. E. Golay (1964), Smoothing and differentiation of data by simplified least squares procedures, *Field, C. B.* (1994), Reflectance indices associated with, *Anal. Chem.*, **36**, 1627–1639, doi:10.1021/ac60214a047.
- Shettle, E. P., and R. W. Fenn (1979), Models for the aerosols of the lower atmosphere and the effects of humidity variations on their optical properties, AFGL-TR-79-0214.
- Smirnov, A., B. N. Holben, T. F. Eck, O. Dubovik, and I. Slutsker (2000), Cloud-screening and quality control algorithms for the AERONET database, *Remote Sens. Environ.*, **73**, 227–349, doi:10.1016/S0034-4257(00)00109-7.
- Tsay, F., and W. Philpot (1998), Derivative analysis of hyperspectral data, *Remote Sens. Environ.*, **66**, 41–51, doi:10.1016/S0034-4257(98)00032-7.
- Tsay, S., et al. (2013), From BASE-ASIA toward 7-SEAS: A satellite-surface perspective of boreal spring biomass-burning aerosols and clouds in Southeast Asia, *Atmos. Environ.*, **78**, 20–34, doi:10.1016/j.atmosenv.2012.12.013.
- Tufillaro, N. B., and C. O. Davis (2012), Derivative spectroscopy with HICO, *Proc. Opt. Remote Sensing Environ.*, doi:10.1364/ORSE.2012.RTu2E.5.
- Twitty, J. T., and J. Weinman (1971), Radiative properties of carbonaceous aerosols, *J. Appl. Meteorol.*, **10**, 725–731.
- Welton, E. J., J. R. Campbell, J. D. Spinhirne, and V. S. Scott (2001), Global monitoring of clouds and aerosols using a network of micro-pulse lidar systems, in *Lidar Remote Sensing for Industry and Environmental Monitoring*, edited by U. N. Singh, T. Itabe, and N. Sugimoto, *Proc. SPIE*, **4153**, 151–158, doi:10.1117/12.417040.
- Winker, D. M., M. A. Vaughan, A. Omar, Y. Hu, K. A. Powell, Z. Liu, W. H. Hunt, and S. A. Young (2009), Overview of the CALIPSO Mission and CALIOP Data Processing Algorithms, *J. Atmos. Oceanic Technol.*, **26**, 2310–2323, doi:10.1175/2009JTECHA1281.1.
- Yang, P., S.-C. Tsay, H. Wei, G. Guo, and Q. Ji (2005), Remote sensing of cirrus optical and microphysical properties from ground-based infrared radiometric measurements-Part I: A new retrieval method based on micro window spectral signature, *IEEE Geosci. Remote Sens. Lett.*, **2**, 128–131, doi:10.1109/LGRS.2005.844733.